PHYSICAL REVIEW B **95**, 195209 (2017)

Point defect segregation and its role in the detrimental nature of Frank partials in Cu(In, Ga)Se$_2$ thin-film absorbers

E. Simsek Sanli,[1] D. Barragan-Yani,[2] Q. M. Ramasse,[3] K. Albe,[2] R. Mainz,[4] D. Abou-Ras,[4]
A. Weber,[4] H.-J. Kleebe,[5] and P. A. van Aken[1]
[1]*Max Planck Institute for Solid State Research, Stuttgart Center for Electron Microscopy, Heisenbergstrasse 1, 70569 Stuttgart, Germany*
[2]*Technische Universität Darmstadt, Institut für Materialwissenschaft, Fachgebiet Materialmodellierung, Jovanka-Bontschits-Strasse 2, 64287 Darmstadt, Germany*
[3]*SuperSTEM Laboratory, SciTech Daresbury Campus, Keckwick Lane, Daresbury WA4 4AD, United Kingdom*
[4]*Helmholtz-Zentrum Berlin für Materialien und Energie GmbH, Hahn-Meitner-Platz 1, 14109 Berlin, Germany*
[5]*Technische Universität Darmstadt, Fachgebiet Geomaterialwissenschaft, Schnittspahnstrasse 9, 64287 Darmstadt, Germany*

(Received 11 September 2016; revised manuscript received 17 February 2017; published 26 May 2017)

The interaction of point defects with extrinsic Frank loops in the photovoltaic absorber material Cu(In, Ga)Se$_2$ was studied by aberration-corrected scanning transmission electron microscopy in combination with electron energy-loss spectroscopy and calculations based on density-functional theory. We find that Cu accumulation occurs outside of the dislocation cores bounding the stacking fault due to strain-induced preferential formation of $\mathrm{Cu}_{\mathrm{In}}^{-2}$, which can be considered a harmful hole trap in Cu(In, Ga)Se$_2$. In the core region of the cation-containing α-core, Cu is found in excess. The calculations reveal that this is because Cu on In-sites is lowering the energy of this dislocation core. Within the Se-containing β-core, in contrast, only a small excess of Cu is observed, which is explained by the fact that $\mathrm{Cu}_{\mathrm{In}}$ and Cu_{i} are the preferred defects inside this core, but their formation energies are positive. The decoration of both cores induces deep defect states, which enhance nonradiative recombination. Thus, the annihilation of Frank loops during the Cu(In, Ga)Se$_2$ growth is essential in order to obtain absorbers with high conversion efficiencies.

DOI: 10.1103/PhysRevB.95.195209

Thin-film solar cells with Cu(In, Ga)Se$_2$ (CIGS) absorber layers exhibit record conversion efficiencies of up to 22.6% [1]. Numerous reports have discussed how polycrystalline CIGS-based solar cells can reach such device performances, in spite of the high density of extended, structural defects [2]. The three-stage coevaporation technique [3], in which the CIGS film passes through a Cu-rich ([Cu]/([In]+[Ga]) >1) stage, is known to lead to high efficiencies as well as to the reduction of planar defects (PDs) [4,5]. In a previous study, we have shown that highly symmetric PDs, such as lamellar twin boundaries (TBs) and stacking faults (SFs), are present in both growth-interrupted—where the process stopped before reaching the Cu-rich stage—as well as growth-finished absorbers [6]. We have also found irregular-complex PDs with cation redistribution present only in the growth-interrupted absorbers. Since highly symmetric PDs are present in growth-finished absorbers and do not substantially affect the electrical properties of the photovoltaic absorber [7,8], PD annihilation would be beneficial only if other types of defects disappear, i.e., irregular PDs that do induce significant changes in the density of states (DOS) relative to the bulk [4].

To reveal why the PD annihilation appears to be beneficial, in this study we provide close insights into the structural, chemical, and electronic properties of a specific type of such complex defects, namely a Frank dislocation loop, observed in a sample obtained from an interrupted CIGS deposition process. To do so, we performed scanning transmission electron microscopy (STEM) analysis and density-functional theory (DFT) calculations of such defect. We find that Frank dislocation loops have detrimental effects on the electronic structure of CIGS, revealing the importance of the planar defect annihilation for the growth of CIGS absorber films for high-efficiency solar cells.

The investigated CIGS absorber layer was deposited by a growth-interrupted three-stage coevaporation process. In the first stage, In and Ga were deposited sequentially under Se atmosphere at 330 °C. This resulted in an In-Se/Ga-Se stack. In the second stage, the substrate temperature was increased to 430 °C. The process continued with Cu deposition under Se atmosphere. We intentionally interrupted the three-stage process during this second stage, before reaching the Cu-rich composition, in order to obtain high defect concentrations [9,10]. The continuation of the process with a Cu-rich stage is known to reduce the density of PDs [4,6]. Up to the point of interruption, the sample was processed like a fully working solar cell, but we did not continue with the Cu-rich stage and subsequent In-Ga-Se deposition (third stage), the buffer and window layers deposition.

Cross-sectional TEM lamellae from the CIGS thin films were prepared with a Zeiss Crossbeam 1540XB focused ion beam (FIB) machine using the lift-out method [11,12]. Sample preparation artifacts were carefully minimized by following an established procedure for producing high-quality samples for low-voltage high-resolution microscopy observation [13]. Structural analysis with atomic resolution was performed using high-resolution STEM (HR-STEM) and electron energy-loss spectroscopy (EELS) [14], providing insights into the atomic arrangements in and around the dislocation cores. A Cs-corrected Nion UltraSTEM 100, equipped with a cold field emission gun (CFEG), was operated at 100 kV acceleration voltage for the HR-STEM investigations [15]. The microscope is equipped with a Gatan Enfina spectrometer for the EEL spectrum imaging, i.e., the acquisition of a three-dimensional data cube with both spatial and spectral information about the selected region. A dispersion of 1 eV/channel was used to cover an energy-loss range from 315 to 1655 eV, allowing for the simultaneous elemental mapping of the Cu $L_{2,3}$, In $M_{4,5}$, Ga $L_{2,3}$, and Se $L_{2,3}$ edges.

Theoretical calculations are done based on DFT as implemented in the VASP [16] simulation package. We used the Dudarev version [17] of LDA+U as the exchange-correlation approximation using $U = 6$ eV for the d-states of Cu. With this setup, the d-like valence-band resonances agree with photoemission measurements giving us the correct position for the valence-band maximum (VBM) [18]. Furthermore, this setup together with band-gap and finite-size corrections has been used successfully for modeling point defects in CIGS [19]. We used projector augmented-wave potentials (PAWs) for the effective potential due to the nucleus and the core electrons. A plane-wave energy cutoff of 350 eV was applied. Atomic relaxations were performed with a single k-point, and the local density of states (LDOS) is calculated using a converged $4\times2\times2$ k-mesh for a supercell of $CuInSe_2$ (CIS) containing 800 atoms. The LDOS was calculated for those atoms contained in a cylinder with a diameter of 8 Å around each core. Individual charges of the atoms in the supercells containing the Frank loop were calculated using the Bader charge analysis [20] as implemented in the software of Henkelman and co-workers [21,22]. Elastic dipole tensors of the most relevant point defects in CIS were calculated following the discussion by Freedman *et al.* [23] and using supercells up to 512 atoms with a k-point grid of $2\times2\times2$. We performed our study only for CIS to be consistent with experiments, due to the fact that the defect was localized in the Ga-poor region of the sample. Nevertheless, we discuss the validity of our conclusions for the quaternary compound.

Figure 1(a) shows a high-angle annular dark-field (HAADF) image recorded from a grain specifically tilted and oriented so the electron beam would travel along the $[1\bar{1}0]$ direction, in which an extended defect is present. In this projection, the stacking sequence of Se columns along the $\langle 221\rangle$ direction is $\ldots ABCABC\ldots$. In the same figure, it is possible to detect a region with a slightly different stacking between two yellow boxes: $\ldots ABC\mathbf{BA}BC\ldots$. There is an additional B plane, which is further complemented by an A plane. The insertion of an additional plane to the perfect crystal produces an extrinsic SF, whereas the deletion of a lattice plane produces an intrinsic SF. Interestingly, this extrinsic SF terminates within the yellow boxes drawn in the same figure. This termination is only possible due to the presence of partial dislocations separating the faulted regions from the perfect crystal [24].

There are two types of partial dislocations; (i) glissile Shockley partials, which can move by gliding, and (ii) sessile Frank partial dislocations, which cannot glide but climb instead [24]. In the partial dislocations shown in Fig. 1(a), the Burgers vector, $b = \mp 1/6\langle 221\rangle$, is normal to the plane of the fault. As a result, it cannot glide, indicating that this is an extrinsic Frank partial dislocation. Furthermore, similar to the case of silicon [25] and based on its sessile nature and what has been found for planar defects in CIS occurring on low-energy facet planes [26], it can be concluded that this is a grown-in defect and not the result of mechanical strain relaxation.

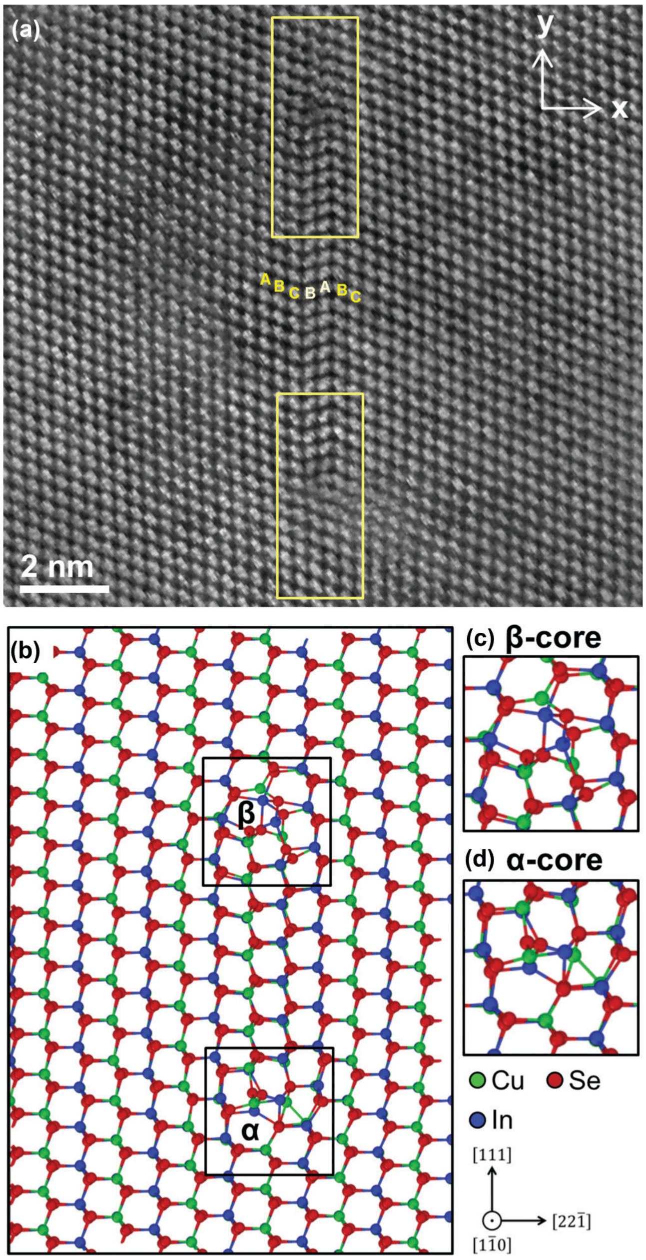

FIG. 1. (a) HAADF image of the positive Frank partial dislocations associated with an extrinsic SF. Two yellow boxes indicate the top and bottom parts of the SF including partial dislocation cores (β-core in the upper box and α-core in the bottom one). Relaxed structure of an extrinsic Frank loop in CIS obtained with DFT. (b) Complete supercell showing the simulated loop, (c) β-core, and (d) α-core.

To study the properties of this Frank loop by means of DFT calculations, a corresponding supercell with a SF bounded by two straight Frank partials was built. As the observed defect was localized in the Ga-poor region of the sample, the simulations were carried out for a CIS structure. This configuration allows us to study a slice of an extrinsic Frank loop, and its relaxed structure can be seen in Fig. 1(b). All atoms are fully coordinated, and no dangling bonds are found. Due to the symmetry of the chalcopyrite structure of CIS and its slip plane (112), in which this defect occurs, any transversal cut of a stoichiometric Frank loop in this material will consist of two structurally different transversal sections of the Frank

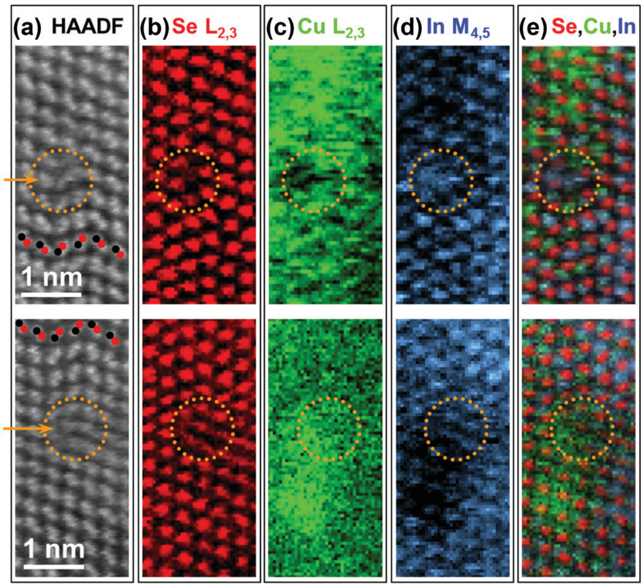

FIG. 2. (a) Two simultaneously acquired HAADF images from the areas indicated by yellow boxes in Fig. 1(a) show the association of the SF and the Frank loop (β-core in the upper panels and α-core in the bottom ones). Dislocation cores are indicated by orange circles on the image. (b)–(d) Corresponding Se $L_{2,3}$, Cu $L_{2,3}$, and In $M_{4,5}$ elemental distribution maps are shown in red, green, and blue. (e) The red-green-blue composite map is a color-coded superposition of the individual elemental maps.

partial bounding the loop, an α- and a β-core, and the extrinsic stacking fault between them. The inserted plane terminates in anions for the β-core [Fig. 1(c)] and in cations for the α-core [Fig. 1(d)].

The two regions indicated by the yellow boxes in Fig. 1(a) were also analyzed by means of EELS, with the HAADF intensity distributions acquired simultaneously with the spectrum images. In this $[1\bar{1}0]$ projection shown in Fig. 2(a), closely spaced Se and alternating In/Ga and Cu columns are visualized as an inset with red (Se) and black (Cu and In/Ga) balls. Se, Cu, and In elemental distribution maps were extracted from the acquired EEL spectra, and they are shown in Figs. 2(b)–2(d) in red, green, and blue, respectively (the intensities were normalized to range from 0 to 1 for simplicity and should therefore not be taken as a quantitative indication of the local chemical composition). Figure 2(e) shows a composite red-green-blue (RGB) image for visual conciseness. Note that no Ga map is presented since, as mentioned above, this dislocation loop was localized in the Ga-poor region of the sample. This made the extraction of the low-intensity Ga $L_{2,3}$ edge, which also overlaps with the Cu $L_{2,3}$ edge, not reliable. The positions of the In and Se columns fit well to the HAADF image atomic column positions. More importantly, Cu-rich clouds were found outside of both cores coinciding with a lower In signal intensity. Directly at the dislocation cores, however, the α-core shows a considerable excess of Cu, while the β-core exhibits only a slight increase in the Cu signal compared to the bulk material. Furthermore, immediately below the cores and to the side of the SF, a subtle drop in Cu signal is seen to coincide with a small increase in In.

To understand such atomic rearrangements, we studied the chemical decoration of Frank partials by means of relative formation energies, defined as

$$E^{q}_{\mathrm{RFE}} = \Delta E_{\mathrm{def}} + \sum_{i} n_i \mu_i + q[E_{\mathrm{F}} + \epsilon_{\mathrm{VBM}}]. \qquad (1)$$

Here ΔE_{def} is the calculated energy difference between the supercell containing a nonstoichiometric Frank loop with a given point defect with charge q located at one of the cores and the stoichiometric Frank loop supercell. The term $\sum_i n_i \mu_i$ accounts for the energetic cost of creating or deleting n atoms of the species i when the point defect is created and $\mu_i = \mu_i^{\mathrm{ref}} + \Delta\mu_i$ is the chemical potential of the element i. The electron reservoir is defined through the VBM energy of the bulk material, ϵ_{VBM}, and the Fermi energy given with respect to the VBM, E_{F}. Finite-size corrections regarding the interaction between localized charges in a neutralizing background and the alignment between the electrostatic potentials of the bulk and the supercell containing the defect were applied following Pohl *et al.* [27]. In our calculations, atomic relaxations were allowed for all calculated defect structures. Nonstoichiometric Frank loop supercells were constructed by creating relevant point defects in the positions indicated by yellow circles in both Figs. 3(a) and 3(b) in the case of the Cu vacancy and antisite defects ($\mathrm{Cu_{In}}$ and $\mathrm{In_{Cu}}$), while the X's mark the position chosen for Cu interstitials. Defect complexes with Cu vacancies were not included in our analysis, since previous calculations have shown that the formation energy of such complexes is higher than the ones of the individual point defects. Since the sample had time to reach thermodynamic equilibrium, the observed defect segregation to dislocations can be interpreted solely based on the calculated formation energies without explicit consideration of the defect kinetics.

The relative formation energies for various defect types in the α-core and β-core are shown in Figs. 3(c) and 3(d), respectively. The chemical potential for Cu was chosen to mimic the experimental Cu-poor conditions $\Delta\mu_{\mathrm{Cu}} = -0.4$ eV. Although the In chemical potential was varied between the limiting values $-1.68 \leqslant \Delta\mu_{\mathrm{In}} \leqslant -1.0$ eV of the stability region of the chalcopyrite phase for $\Delta\mu_{\mathrm{Cu}} = -0.4$ eV (see Ref. [27] for details), our analysis is focused on the case in which $\Delta\mu_{\mathrm{In}} \simeq -1.0$ eV in which the system is close to the experimental conditions. In addition, we assume a Fermi level position close to the VBM. Relative formation energies of charged defects are presented as colored bands reflecting the range of possible Fermi levels ($0 \leqslant E_{\mathrm{F}} \leqslant 0.25$ eV).

In the cation-containing α-core, Fig. 3(c), the neutral and charged $\mathrm{Cu_{In}}$ antisites exhibit negative formation energies, which means that this defect would occur spontaneously and that the α-core has a tendency to be decorated by excess Cu. Within the relevant range of Fermi energies, the neutral antisite is the most stable configuration. Thus the Cu-rich dislocation core has no excess charge. Only when E_{F} is extremely close to the VBM does the $\mathrm{In_{Cu}}$ antisite also have a negative E^{q}_{RFE} and could occur. Since these thermodynamic conditions do not occur in the real absorber, we can conclude that the decoration of the α-core by neutral $\mathrm{Cu_{In}}$ is the main reason for the considerable Cu accumulation at the α-core observed in experiments.

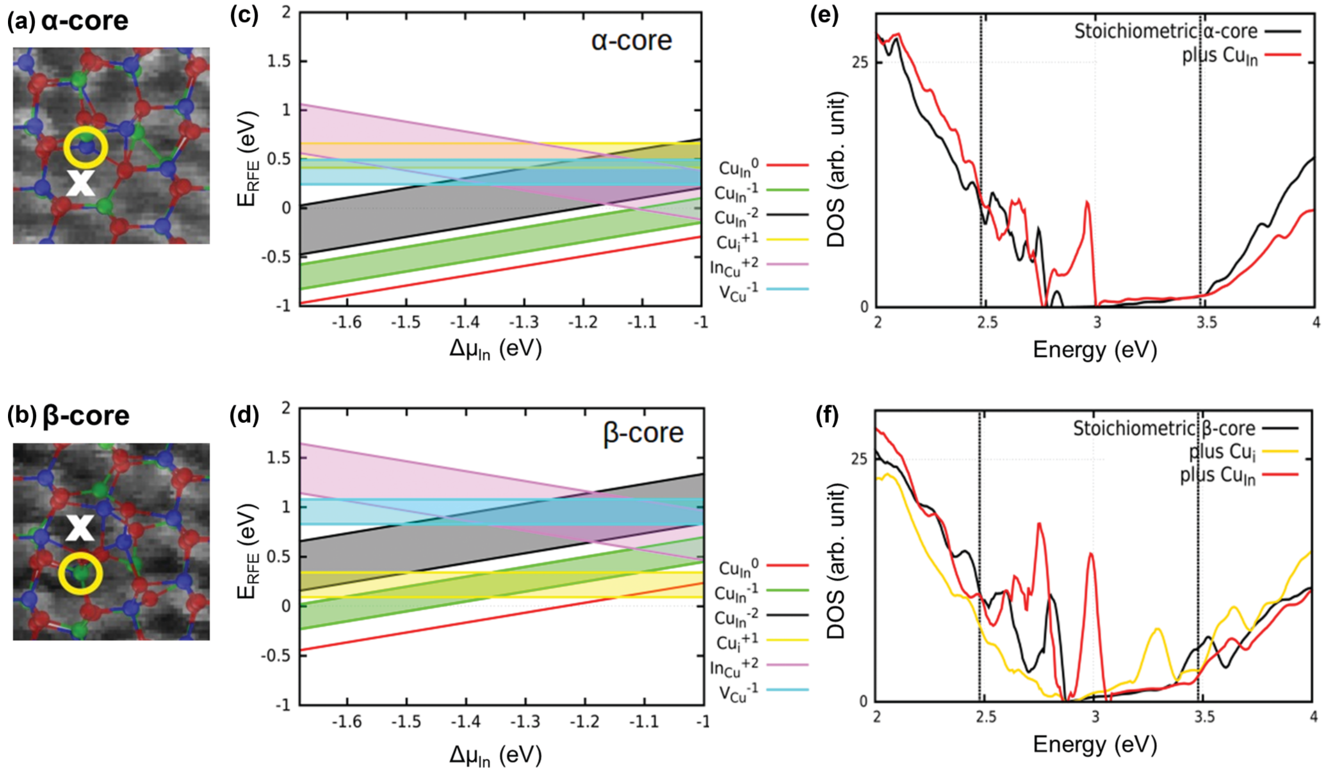

FIG. 3. Simulated structures were superimposed on the HAADF images for the (a) α-core and (b) β-core. Relative formation energies of point defects inside the (c) α- and (d) β-cores of the Frank loop. The chemical potentials for Cu and In were chosen to mimic the experimental Cu-poor conditions, and charged defects are presented as colored bands rather than lines to show also their values when $0 \leqslant E_F \leqslant 0.25$ eV. LDOSs of stoichiometric and decorated cores are shown for both (e) α-core and (f) β-core. The band gap of the bulk structure is marked by dotted vertical lines.

For the Se-containing β-core, Fig. 3(d), all defect structures exhibit positive formation energies when $\Delta\mu_{\mathrm{In}} \simeq -1.0$ eV, which is the reason why compositional changes observed experimentally inside this core are less marked compared to its α counterpart. The presence of the neutral $\mathrm{Cu_{In}}$ antisite and some Cu interstitials explains the slight Cu increase found in this structure.

Therefore, the experimentally observed behavior of Cu at the dislocation cores, Fig. 2, is in full agreement with our theoretical results. After unraveling the causes of such chemical changes inside the α- and β-cores, we used the LDOS of both structures when decorated with their preferred point defects, Figs. 3(e) and 3(f), to study the effects of such nonstoichiometric structures on the electrical properties of the absorber layer. We found that the presence of $\mathrm{Cu_{In}}$ inside both α- and β-cores induces a defect state around the middle of the gap and enhances nonradiative recombination. Thus, the decorated Frank loop should be electrically active due to the presence of $\mathrm{Cu_{In}}$ inside the α- and β-cores. Moreover, although there are no dangling bonds in the stoichiometric structures, defect levels are also observed in the LDOS of the stoichiometric structures. We argue that they are strain-induced, similar to what has been observed in the case of threading dislocations in GaN [28].

To elucidate the nature of the Cu clouds detected around the cores (Fig. 2), further HAADF and EELS experiments were conducted. Over a larger field of view, such results obtained on other, similar line defects showed Cu clouds that extend up to 10 nm away from the dislocation cores (see the Supplemental Material [29]). The absence of dangling bonds in the relaxed stoichiometric structures and the resulting absence of localized charges rules out electrostatic interaction, which is in contrast to the case of full dislocations reported by Dietrich *et al.* [30]. The nonsymmetric distribution of the Cu clouds around the dislocations also provides a hint that they cannot be due to electrostatic potentials, which would imply only a radial dependence of Cu distribution.

Therefore, we tested if strain is a possible driving force of such atomic redistribution around the cores. Geometrical phase analysis (GPA) [31] was used to visualize the compressive and tensile strain fields associated with the dislocation cores. The main x and y axes, chosen for the strain analysis, are presented on the HAADF image in Fig. 1(a). Figures 4(a) and 4(b) show the corresponding components, ε_{xx} and ε_{yy}, of the strain tensor superimposed to the same HAADF image (with a 90° rotation to the left) to correlate visually the measured strain values to the exact atomic positions. The color bar indicates a change in strain from +5% tensile to −5% compressive for both the ε_{xx} and ε_{yy} components. The atoms at the SF, especially those near the dislocation cores, experience compressive strain. At the sides of the SF, the effect is inverted, and atoms experience tensile strain. At the SF, the atomic columns are displaced horizontally from their positions, larger distances away from the dislocation cores along the x direction. It results in larger strain fields as is shown in the ε_{xx} map. In contrast, the vertical displacement is rather localized close to the dislocation

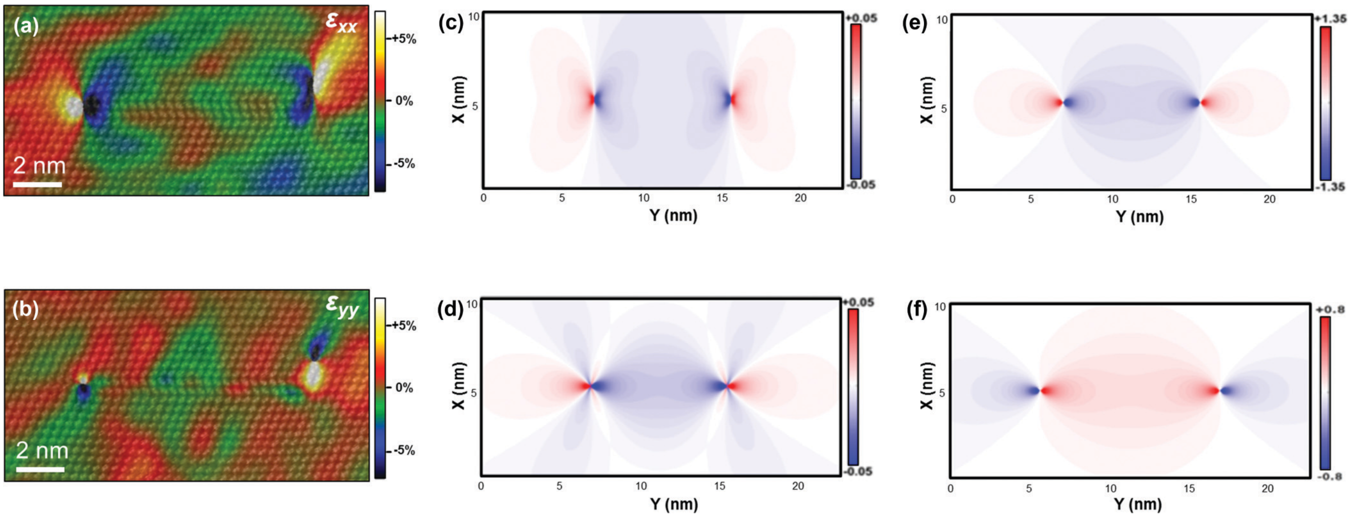

FIG. 4. The HAADF image shown in Fig. 1(a) is superimposed with (a) ε_{xx} and (b) ε_{yy} strain components extracted by GPA. Strain fields for an extrinsic Frank loop as predicted from linear elasticity solutions (c) ε_{xx} and (d) ε_{yy} and the $n_d \sum_{ij} \epsilon_{ij} G_{ij}$ term in eV for the (e) $\mathrm{Cu}_{\mathrm{In}}^{-2}$ and (f) $\mathrm{In}_{\mathrm{Cu}}^{+2}$ antisites.

core in the y direction. For comparison we calculated the strain field components for a pair of partial dislocations, ε_{xx} and ε_{yy}, from linear elasticity [24]. In Figs. 4(c) and 4(d) the theoretical strain distribution is shown, which reproduces the experimental result. Similarities in the positioning of the tensile and compressive regions between theoretical and experimental results give us further proof that the defect studied with HR-STEM is indeed an extrinsic Frank loop. Since linear elastic results are divergent, very close to the core we bound the results to a maximum of ±5%. To reveal the nature of the Cu clouds, we analyzed the mechanical coupling of this strain field to the defect thermodynamics. The defect formation energy in a material subject to a strain field with components $\epsilon_{ij}(\vec{r})$ can be obtained from the formation energy of the unstrained state ΔE_o^f and the elastic dipole tensors G_{ij} from the relation $\Delta E^f(\epsilon_{ij}) = \Delta E_o^f - \sum_{ij} \epsilon_{ij}(\vec{r}) G_{ij}$.

The formation energy of a defect would decrease only if the term $\sum_{ij} \epsilon_{ij}(\vec{r}) G_{ij}$ is positive. We have calculated the defect dipole tensors for various point defects (see the Supplemental Material [29]) for their relevant charge states. The largest positive G_{ij}'s are found for the $\mathrm{Cu}_{\mathrm{In}}^{-2}$ antisite, and therefore it is the preferred defect in areas under tensile strain. On the other hand, $\mathrm{In}_{\mathrm{Cu}}^{+2}$ antisites exhibit the largest negative G_{ij}'s and hence could be expected to occur in areas under compressive strain. As a quantitative example, Figs. 4(e) and 4(f) show the values of $\sum_{ij} \epsilon_{ij} G_{ij}$ for $\mathrm{Cu}_{\mathrm{In}}^{-2}$ and $\mathrm{In}_{\mathrm{Cu}}^{+2}$ antisites, when immersed in the theoretical strain field presented in Figs. 4(c) and 4(d). The maximum change in formation energy due to strain for such antisites is around 1.51 eV for the $\mathrm{Cu}_{\mathrm{In}}^{-2}$ and 0.65 eV for the $\mathrm{In}_{\mathrm{Cu}}^{+2}$, which are of the order of the formation energies of these defect types. Therefore, the massive excess Cu clouds are likely caused by strain-driven accumulation of such defects. Charge accumulation associated with an excess of $\mathrm{Cu}_{\mathrm{In}}^{-2}$ must be compensated, which may be satisfied through the presence of $\mathrm{In}_{\mathrm{Cu}}^{+2}$ antisites, creating a positively charged In-area directly opposite the Cu clouds. The EELS maps show a few atomic columns below the cores and to the side of the SF (in the compressive region) where a slight increase in the In signal is accompanied by a decrease in Cu, pointing out the presence of the expected $\mathrm{In}_{\mathrm{Cu}}^{+2}$ antisites.

Regarding the effect of such clouds on the electrical properties of a device containing dislocation loops like the one studied here, it has been pointed out in previous studies that the $\mathrm{Cu}_{\mathrm{In}}^{-2}$ antisite constitutes the most harmful hole-trap in CIGS absorber layers [27]. Thus, Cu clouds composed of such defects would also be detrimental for the efficiency of the device.

In the case of the quaternary compound CIGS, conclusions can be drawn by including Ga in our analysis. In such a situation, the expected In-rich clouds would include $\mathrm{Ga}_{\mathrm{Cu}}^{+2}$ along with $\mathrm{In}_{\mathrm{Cu}}^{+2}$, since both would respond similarly to strain due to the analogous ionic radius of In and Ga. It was shown that both $\mathrm{Ga}_{\mathrm{Cu}}^{+2}$ along with $\mathrm{In}_{\mathrm{Cu}}^{+2}$ are shallow donor defects [27]. Therefore, our finding that the presence of $\mathrm{Cu}_{\mathrm{In}}$ is the factor determining the detrimental nature would remain valid for CIGS.

In conclusion, we have elucidated the structure and chemistry of Frank loops in CIGS thin films at atomic resolution, and we have correlated them with DFT simulations. Our EELS and DFT results suggest that inside the cores, asymmetric Cu excess occurs depending on the structurally caused cation or anion excess in α- and β-cores, respectively. We found that the considerable Cu excess observed in the α-core is due to the presence of neutral $\mathrm{Cu}_{\mathrm{In}}^{0}$ antisites, which have a negative formation energy and therefore may form spontaneously. In the case of the β-core, the slight Cu excess is explained by the presence of both neutral $\mathrm{Cu}_{\mathrm{In}}$ and Cu interstitials, which have low positive formation energies inside the β-core. Evidence is provided that the formation of the Cu clouds detected outside of the core region, which probably consist of $\mathrm{Cu}_{\mathrm{In}}^{-2}$ point defects, is driven by the interaction of the strain fields of the dislocations with the point defects.

Also due to strain, $\mathrm{In}_{\mathrm{Cu}}^{+2}$ antisites are predicted to accumulate in areas under compressive strain, providing a charge-compensation mechanism. Although not as prominent as the Cu-rich clouds, they are observed by means of EELS. Since the calculated energy band diagrams suggest that the presence of $\mathrm{Cu_{In}}$ at the α- and β-cores induces deep midgap defect states, the annihilation of Frank loops during the CIGS growth is essential in order to obtain high absorber qualities for record conversion efficiencies of the corresponding solar-cell devices.

The authors thank Bernhard Fenk for FIB sample preparation and Wilfried Sigle for discussions. The work was supported in part by the Helmholtz Virtual Institute HVI-520 “Microstructure Control for Thin-Film Solar Cells”, by the European Union Seventh Framework Program (FP/2007-2013) under Grant Agreement No. 312483 (ESTEEM2), as well as by the European Metrology Research Programme (EMRP) Project IND07 Thin Films. The EMRP is jointly funded by the EMRP participating countries within EURAMET and the European Union. SuperSTEM is the UK National Facility for Aberration-Corrected STEM, funded by EPSRC. D.B. and K.A. gratefully acknowledge the computing time granted by the John von Neumann Institute for Computing (NIC) and provided on the supercomputer JURECA at Jülich Supercomputing Centre (JSC). Moreover, computing time was granted on the Lichtenberg High-Performance Computer at TU Darmstadt.

E.S.S. and D.B.Y. contributed equally to this work.

---

[1] P. Jackson, R. Wuerz, D. Hariskos, E. Lotter, W. Witte, and M. Powalla, Phys. Status Solidi Rapid Res. Lett. **10**, 583 (2016).

[2] D. Abou-Ras, S. S. Schmidt, N. Schaefer, J. Kavalakkatt, T. Rissom, T. Unold, R. Mainz, A. Weber, T. Kirchartz, E. Simsek Sanli, P. A. van Aken, Q. M. Ramasse, H.-J. Kleebe, D. Azulay, I. Balberg, O. Millo, O. Cojocaru-Mirédin, D. Barragan-Yani, K. Albe, J. Haarstrich, and C. Ronning, Phys. Status Solidi Rapid Res. Lett. **10**, 363 (2016).

[3] A. M. Gabor, J. R. Tuttle, D. S. Albin, M. A. Contreras, R. Noufi, and A. M. Hermann, Appl. Phys. Lett. **65**, 198 (1994).

[4] R. Mainz, E. S. Sanli, H. Stange, D. Azulay, S. Brunken, D. Greiner, S. Hajaj, M. D. Heinemann, C. A. Kaufmann, M. Klaus, Q. M. Ramasse, H. Rodriguez-Alvarez, A. Weber, I. Balberg, O. Millo, P. A. van Aken, and D. Abou-Ras, Energy Environ. Sci. **9**, 1818 (2016).

[5] H. Stange, S. Brunken, H. Hempel, H. Rodriguez-Alvarez, N. Schaefer, D. Greiner, A. Scheu, J. Lauche, C. A. Kaufmann, T. Unold, D. Abou-Ras, and R. Mainz, Appl. Phys. Lett. **107**, 152103 (2015).

[6] E. S. Sanli, Q. M. Ramasse, W. Sigle, D. Abou-Ras, R. Mainz, A. Weber, H.-J. Kleebe, and P. A. van Aken, J. Appl. Phys. **120**, 205301 (2016).

[7] Y. Yan, K. M. Jones, C. S. Jiang, X. Z. Wu, R. Noufi, and M. M. Al-Jassim, Physica B **401-402**, 25 (2007).

[8] H. Mirhosseini, J. Kiss, and C. Felser, Phys. Rev. Appl. **4**, 064005 (2015).

[9] S. Nishiwaki, T. Satoh, S. Hayashi, Y. Hashimoto, T. Negami, and T. Wada, J. Mater. Res. **14**, 4514 (1999).

[10] H. Rodriguez-Alvarez, N. Barreau, C. A. Kaufmann, A. Weber, M. Klaus, T. Painchaud, H. W. Schock, and R. Mainz, Acta Mater. **61**, 4347 (2013).

[11] L. A. Giannuzzi, J. L. Drown, S. R. Brown, R. B. Irwin, and F. A. Stevie, Microsc. Res. Technol. **41**, 285 (1998).

[12] M. H. F. Overwijk, F. C. van den Heuvel, and C. W. T. Bulle-Lieuwma, J. Vac. Sci. Technol. B **11**, 2021 (1993).

[13] M. Schaffer, B. Schaffer, and Q. Ramasse, Ultramicroscopy **114**, 62 (2012).

[14] R. Egerton, *Electron Energy-Loss Spectroscopy in the Electron Microscope* (Springer, New York, 2011).

[15] O. L. Krivanek, G. J. Corbin, N. Dellby, B. F. Elston, R. J. Keyse, M. F. Murfitt, C. S. Own, Z. S. Szilagyi, and J. W. Woodruff, Ultramicroscopy **108**, 179 (2008).

[16] G. Kresse and J. Furthmüller, Comput. Mater. Sci. **6**, 15 (1996).

[17] S. L. Dudarev, G. A. Botton, S. Y. Savrasov, C. J. Humphreys, and A. P. Sutton, Phys. Rev. B **57**, 1505 (1998).

[18] L. Ley, R. A. Pollak, F. R. McFeely, S. P. Kowalczyk, and D. A. Shirley, Phys. Rev. B **9**, 600 (1974).

[19] C. Persson, Y.-J. Zhao, S. Lany, and A. Zunger, Phys. Rev. B **72**, 035211 (2005).

[20] R. F. W. Bader, *Atoms in Molecules—A Quantum Theory* (Oxford University Press, Oxford, 1990).

[21] G. Henkelman, A. Arnaldsson, and H. Jonsson, Comput. Mater. Sci. **36**, 354 (2006).

[22] E. Sanville, S. D. Kenny, R. Smith, and G. Henkelman, J. Comput. Chem. **28**, 899 (2007).

[23] D. A. Freedman, D. Roundy, and T. A. Arias, Phys. Rev. B **80**, 064108 (2009).

[24] D. Hull and D. Bacon, *Introduction to Dislocations* (Elsevier Science, Oxford, UK, 2001).

[25] H. Foll and B. O. Kolbesen, Appl. Phys. **8**, 319 (1975).

[26] C. J. Kiely, R. C. Pond, G. Kenshole, and A. Rockett, Philos. Mag. A **63**, 1249 (1991).

[27] J. Pohl and K. Albe, Phys. Rev. B **87**, 245203 (2013).

[28] L. Lymperakis, J. Neugebauer, M. Albrecht, T. Remmele, and H. P. Strunk, Phys. Rev. Lett. **93**, 196401 (2004).

[29] See Supplemental Material at http://link.aps.org/supplemental/10.1103/PhysRevB.95.195209 for a similar line defect over a large field of view; calculated defect dipole tensor for various point defects.

[30] J. Dietrich, D. Abou-Ras, S. S. Schmidt, T. Rissom, T. Unold, O. Cojocaru-Mirédin, T. Niermann, M. Lehmann, C. T. Koch, and C. Boit, J. Appl. Phys. **115**, 103507 (2014).

[31] M. J. Hÿtch, E. Snoeck, and R. Kilaas, Ultramicroscopy **74**, 131 (1998).